Optimization of photophoretic forces in coated-hollow microspheres

D.J.S. Pereira, M.R.O. Panão*

ADAI, LAETA, Dept. of Mechanical Engineering, University of Coimbra, Portugal
*Corresponding author: miguel.panao@dem.uc.pt

Keywords: Photophoresis, Optics, Slip-flow, Heat transfer.

ABSTRACT

Photophoresis, a thermal phenomenon, generates non-contact forces on microparticles in a fluid when exposed to a light beam, such as a laser. These forces depend on the geometrical, thermal, and optical properties of the particles, and aligning these properties in inhomogeneous particles can enhance photophoretic forces. The use of coated-hollow microspheres offers a promising approach to this challenge. This work presents a photophoresis model for a three-layered microsphere in the slip-flow regime, applying Navier-Stokes equations with corrected boundary conditions. We used numerical approaches to compute the heat source function q_g using Lorenz-Mie theory and validated the results against previous works. Applied to a copper-coated glass bubble, the model analyzed the photophoretic force as a function of coating thickness, considering several shell thicknesses. Results show that nanometric scale coatings enhance the force up to a maximum, after which the high thermal conductivity of copper reduces it. For coatings above $100\ nm$, the force becomes insensitive to shell thickness, demonstrating copper's dominance in optical and thermal phenomena. The study suggests depositing excess coating for higher photophoretic forces, providing a framework for optimizing microparticle design for photophoretic applications. Future work includes further validation through numerical models and experiments and finding analytical solutions for integrals associated with terms in the boundary coefficients using Lorenz-Mie Theory, which holds great promise for advancing our understanding of photophoresis.

1. Introduction

Photophoresis is a particle-light-induced phenomenon with several applications, such as volumetric displays, which use photophoretic trapping techniques. Photophoretic traps excel in handling and controlling absorbing particles with micrometer sizes. Unlike optical tweezer traps that rely on radiation pressure and gradient forces, these traps use thermal forces, mainly through thermal accommodation and thermal creep. The uneven heating of the particle results in a directional force moving away from the high irradiance areas, effectively manipulating the particle's position and movement. Laser light sources are crucial for photophoretic optical traps. The Optical Trap Display (OTD) works by first trapping a micrometre-scale opaque particle in a near-invisible (405-nm wavelength) photophoretic optical trap. Once a particle is confined, the scanned trap allows the particle to move through a volume in the space that it shares with the user. A system of collinear

RGB lasers then illuminates the trapped particle to create a highly saturated, full-color, low-speckle 3D image in space by the persistence of vision (POV) Smalley et al. (2018). Most works on volumetric displays use black liquor particles, but Rogers et al. (2019) suggested their replacement by uniform coated microspheres (Bera et al., 2016), recognizing that particles' characteristics have a significant impact on the display performance.

Researchers developed several models to study the photophoretic force on homogeneous particles, as discussed in Pereira & Panão (2022). These models show that the photophoretic force's magnitude directly correlates with the particle's optical absorptivity and is inversely proportional to its thermal conductivity. To maximize the photophoretic force, a material with high absorptivity and low thermal conductivity would be ideal, though finding such a material can be challenging for specific wavelengths. One way to overcome this difficulty is to use a multilayer particle approach, where the core material has low thermal conductivity, and the coating has adequate absorptivity. However, there is no model for photophoresis of these types of particles found in the literature, even though some optical trap experiments performed by Eckerskorn et al. (2015); Lizana et al. (2018), who considered multilayered microspheres. Most photophoretic modeling focuses on the optical properties of the particle and thermal properties of the surrounding medium, with little attention given to the thermal properties of the particle material(s). Multilayered particles might lead to a customized approach with several advantages.

In this work, we develop a photophoresis model for a three-layered microsphere in the slip-flow regime. In this regime, the Navier-Stokes equations are valid. Still, it is necessary to correct the boundary conditions with appropriate ones for this regime (Brock, 1962; Eckerskorn et al., 2015; Shvedov et al., 2009; Mackowski, 1989) allowing for discontinuities in the temperature and velocity fields. The next section is dedicated to photophoretic modeling, followed by a section applying it to coated glass bubbles (hollow glass microspheres).

2. Photophoresis model

Fig. 1 represents a coated-hollow microsphere subjected to uni-dimensional photophoresis. The microsphere has a hollow core with radius R_1, a shell layer with outer radius R_2, and an absorbing coatingwith outer radius R_3. A uniform light beam travels in the direction of the Oz direction. Due to the axisymmetry of the light beam, the temperature and velocity fields are also axisymmetrical around the Oz axis and only depend on the polar coordinates (r, θ). The coordinate system is centered and moves with the particle.

In photophoresis, the Reynolds number is minimal (Re $\ll 1$) due to the small size of the particles and reduced velocity, expressing an essentially viscous flow. Assuming also constant properties of the air, the Navier-Stokes equations governing the flow surrounding the sphere simplify to:

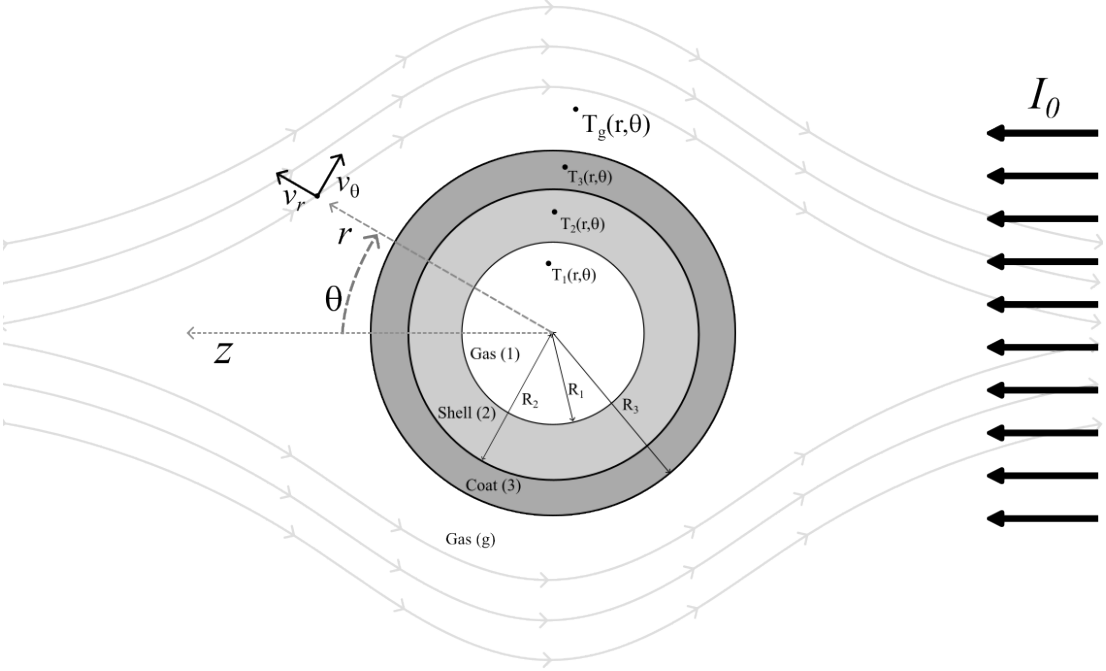

Figure 1. Coated-hollow microsphere representation

$$\nabla P_g(r,\theta) = \mu_g \nabla^2 \overrightarrow{V_g}(r,\theta) \tag{1}$$

$$\nabla \overrightarrow{V_g}(r,\theta) = 0 \tag{2}$$

where P_g is the air pressure, μ_g is the air dynamic viscosity and $\overrightarrow{V_g}$ is the air velocity.

Regarding the temperature fields, calculations include four domains (surrounding environment, coating, shell, and hollow inner volume). A low Reynolds number leads to a low Péclet number in the air, which means that the heat transfer occurs by diffusion in all domains. The general equation that governs heat diffusion assuming constant properties is:

$$\nabla^2 T(r,\theta) = -\frac{q_g(r,\theta)}{k} \tag{3}$$

where $T(r,\theta)$ is the temperature, $q_g(r,\theta)$ is the internal volumetric heat generation (only present in the coatingdomain) in W/m^3. The model developed considers two parts: a thermal one and another related to fluid flow, which is detailed in the following sections.

2.1. Thermal part

Eq. (3) shows that a low Péclet number implies the thermal part does not depend on the flow field. Consequently, one can solve the temperature field first. The solving procedure is a generalization of the method used by Yalamov & Khasanov (1998) for a sphere with uniform thermal conduc-

tivity but now applied to four domains. The general solution to Eq. (3) is given by the following expressions:

$$T(r,\theta) = T_\infty + \sum_{n=0}^{\infty} T_n(r) P_n(\cos\theta) \tag{4}$$

$$T_n(r) = \frac{A_n}{r^{n+1}} + r^n B_n + \frac{1}{(2n+1)k} \times \left[\frac{1}{r^{n+1}} \int_{R_3}^{r} q_{gn}(r) r^{n+2} dr - r^n \int_{R_3}^{r} q_{gn}(r) \frac{dr}{r^{n-1}} \right] \tag{5}$$

$$q_{gn}(r) = \frac{2n+1}{2} \int_0^{\pi} q_g(r,\theta) P_n(\cos\theta) \sin\theta d\theta \tag{6}$$

where A_n and B_n are boundary condition coefficients, T_∞ is the surrounding environment temperature, k is the thermal conductivity of the corresponding medium and P_n are Legendre Polynomials. In the hollow core medium, taking into account that the solution must be finite at $r = 0$ and without heat generation, the solution simplifies to:

$$T_1(r,\theta) = T_\infty + \sum_{n=0}^{\infty} r^n B_{1n} P_n(\cos\theta) \tag{7}$$

In the Shell layer, also without heat generation, the solution simplifies to:

$$T_2(r,\theta) = T_\infty + \sum_{n=0}^{\infty} \left[\frac{A_{2n}}{r^{n+1}} + r^n B_{2n} \right] P_n(\cos\theta) \tag{8}$$

In the coated layer, there are no simplifications, and the solution is:

$$T_3(r,\theta) = T_\infty + \sum_{n=0}^{\infty} T_{3n}(r) P_n(\cos\theta) \tag{9}$$

$$T_{3n}(r) = \frac{A_{3n}}{r^{n+1}} + r^n B_{3n} + \frac{1}{(2n+1)k_3} \times \left[\frac{1}{r^{n+1}} \int_{R_3}^{r} q_{gn}(r) r^{n+2} dr - r^n \int_{R_3}^{r} q_{gn}(r) \frac{dr}{r^{n-1}} \right] \tag{10}$$

In the air region, also taking into account the absence of heat generation and that the solution must be finite at $r \longrightarrow \infty$, it simplifies to:

$$T_g(r,\theta) = T_\infty + \sum_{n=0}^{\infty} \frac{A_{gn}}{r^{n+1}} P_n(\cos\theta) \tag{11}$$

In order to fully solve the temperature fields, one needs to determine the boundary coefficients $B_{1n}, A_{2n}, B_{2n}, B_{3n}, A_{3n}$ and A_{gn}. Expressing the remaining heat flux and temperature boundary conditions at the interfaces $r = R_1, r = R_2$ and $r = R_3$ allows for their determination as:

$$T_2(r,\theta)|_{r=R_1} - T_1(r,\theta)|_{r=R_1} = K_t K n_h R_1 \left.\frac{\partial T_1}{\partial r}\right|_{r=R_1} \tag{12}$$

$$k_1 \left.\frac{\partial T_1(r,\theta)}{\partial r}\right|_{r=R_1} = k_2 \left.\frac{\partial T_2(r,\theta)}{\partial r}\right|_{r=R_1} \tag{13}$$

$$T_2(r,\theta)|_{r=R_2} = T_3(r,\theta)|_{r=R_2} \tag{14}$$

$$k_2 \left.\frac{\partial T_2(r,\theta)}{\partial r}\right|_{r=R_2} = k_3 \left.\frac{\partial T_3(r,\theta)}{\partial r}\right|_{r=R_2} \tag{15}$$

$$T_g(r,\theta)|_{r=R_3} - T_3(r,\theta)|_{r=R_3} = K_t K n R_3 \left.\frac{\partial T_g}{\partial r}\right|_{r=R_3} \tag{16}$$

$$k_g \left.\frac{\partial T_g(r,\theta)}{\partial r}\right|_{r=R_3} = k_3 \left.\frac{\partial T_3(r,\theta)}{\partial r}\right|_{r=R_3} \tag{17}$$

where K_t is the thermal jump coefficient that must be included in the slip-flow regime. The solution to Eqs. (12-17) results in an infinite amount of boundary coefficients. However, as will be discussed later, only the boundary coefficients A_{g0} and A_{g1} are necessary to calculate the photophoretic force. Therefore, the values of A_{g0} and A_{g1} are:

$$A_{g0} = \frac{\int_{R_2}^{R_3}\int_0^{\pi} r^2\, q_g(r,\theta)\sin\theta d\theta dr}{2k_g} \tag{18}$$

$$A_{g1} = \frac{3}{2}\frac{R_3^3(G1\ F1 + G2\ F2)I_0}{k_1(D1+D2) - 2k_2(1+Kn_hK_t)(D3+D4)} \tag{19}$$

$$F1 = \int_{R_2}^{R_3}\int_0^{\pi} r^3\, q_g^*(r,\theta)\cos\theta\sin\theta d\theta dr \tag{20}$$

$$F2 = \int_{R_2}^{R_3}\int_0^{\pi} R_2^3\, q_g^*(r,\theta)\cos\theta\sin\theta d\theta dr \tag{21}$$

where $q_g^* = q_g/I_0$ is the normalized heat source function and the scales ($D1$, $D2$, $D3$, $D4$, $G1$ and $G2$) are in Appendix A.

2.2. Fluid flow part

The solution for the fluid flow part uses the method described by Mackowski (1989), adding the thermal stress slip in the boundary conditions (Chang & Keh, 2012). The general solutions for the pressure and velocity fields described by the hydrodynamic Eqs. (1) and (2) are given by:

$$\overrightarrow{V_g}(r,\theta) = v_r\hat{e}_r + v_\theta\hat{e}_\theta \tag{22}$$

$$v_r = \sum_{n=1}^{\infty} v_{rn}(r)P_n(\mu) \tag{23}$$

$$v_\theta = \sum_{n=1}^{\infty} v_{\theta n}(r)P_n^{(1)}(\mu) \tag{24}$$

$$P = \sum_{n=1}^{\infty} p_n(r)P_n(\mu) \tag{25}$$

where $v_{rn}(r), v_{\theta n}(r)$ and $p_n(r)$ are undetermined functions of r and $P_n^{(1)}(\mu)$ are the associated Legendre polynomials of the first order. When integrating the stress tensor throughout the sphere surface to determine the applied force, all terms vanish except $n = 1$ due to the orthogonality properties of the Legendre polynomials. The fluid flow field problem becomes a simple case of Stokes flow past a sphere, where the velocity components are given by:

$$v_r = V_0\left(1 - \frac{2C_1}{r} + \frac{2C_2}{r^3}\right)\cos\theta \tag{26}$$

$$v_\theta = -V_0\left(1 - \frac{C_1}{r} - \frac{C_2}{r^3}\right)\sin\theta \tag{27}$$

with C_1 and C_2 as boundary coefficients and V_0 as the undisturbed flow velocity relative to the coordinate system. The following boundary conditions allow determining the boundary coefficients for slip-flow (Loesche & Husmann, 2016):

$$v_r = 0, r = R_3 \tag{28}$$

$$v_\theta = K_m Kn R_3\left(r\frac{\partial}{\partial r}\left(\frac{v_\theta}{r}\right) + \frac{1}{r}\frac{\partial v_r}{\partial\theta}\right) + \frac{K_{TS}\mu_g}{\rho_g T_{gS} R_3}\frac{\partial T_g}{\partial\theta} - \frac{K_m Kn K_h R_3\mu_g}{\rho_g T_{gS}}\left(\frac{1}{r}\frac{\partial^2 T_g}{\partial r\partial\theta} - \frac{1}{r^2}\frac{\partial T_g}{\partial\theta}\right), r = R_3 \tag{29}$$

where T_{gS} is the average gas temperature at the particle surface, K_{TS} is the thermal creep coefficient, K_m is the gas-kinetic frictional slip coefficient, and K_h is the thermal slip coefficient, which is present in the terms describing the thermal creep, frictional slip, and thermal stress slip, respectively. From the Stokes flow simplification, the force acting on the particle is given by $F = 8\pi R_3\mu_g V_0 C_1$, and the C_1 coefficient by:

$$C_1 = \frac{3}{4}\frac{1 + 2K_m Kn}{1 + 3K_m Kn} - \frac{1}{2}\frac{(3K_h K_m Kn + K_{TS})\mu_g}{(1 + 3K_m Kn)R_3^3 T_{gS} V_0\rho_g}A_{g1} \tag{30}$$

where the first term describes the Stokes drag with slip-flow correction, and the second term represents the photophoretic force:

$$F_{ph} = -\frac{4\pi\mu_g^2(3K_h K_m Kn + K_{TS})}{(1 + 3K_m Kn)R_3^2 T_{gS}\rho_g}A_{g1} \tag{31}$$

The value of T_{gS} can be determined using Eq. (11) and the properties of Legendre polynomials, resulting in:

$$T_{gS} = T_\infty + \frac{A_{g0}}{R_3} \tag{32}$$

3. Model validation

The next step is model validation, where the photophoretic force predicted by the developed analytical model is compared against results from a CFD software, in this case, ANSYS FLUENT. At this stage, the model is validated for larger particles (Continuum regime, $Kn \longrightarrow 0$) because smaller particles present some challenges for the software.

The arbitrary test particle has radiuses $R_1 = 40\mu m$, $R_2 = 50\mu m$ and $R_3 = 55\mu m$. The thermal conductivities of each domain are $k_1 = 0.0262W \cdot m^{-1}K^{-1}$, $k_2 = 1W \cdot m^{-1}K^{-1}$ and $k_3 = 10W \cdot m^{-1}K^{-1}$. The gas properties are $T_\infty = 300K$, $k_g = 0.0262W/(mK)$, $\rho_g = 1.225kg/m^3$ and $\mu_g = 17.894\mu Pa\ s$. The arbitrary particle is perfectly absorbing, which leads to an internal heat generation given by:

$$q_g(r,\theta) = \begin{cases} \dfrac{I_0 \cos(\pi - \theta)}{\delta} & \text{if } z \leq 0, R_p - \delta < r \leq R_p \\ 0 & \text{if } z > 0 \end{cases} \tag{33}$$

where δ is the absorption thickness and $\delta \longrightarrow 0$. Because the value of δ needs to be finite for the simulations, the absorption thickness was assumed to be $1nm$. Similarly to the model development, the validation is also divided into a thermal and fluid flow part.

3.1. Thermal part

The thermal part of the model ultimately leads to the determination of the coefficients A_{g0} and A_{g1}, which describe the temperature distribution in the gas domain. For the thermal part validation, these coefficients were first calculated analytically for the arbitrary particle chosen. For the numerical comparison, the modeling with Ansys Fluent for the same particle in the same conditions allowed obtaining the results for the temperature distribution in the gas domain. The gas temperature surrounding the particle is given by Eq. (11), which can be expanded as:

$$T_g(r,\theta) \approx T_\infty + \frac{A_{g0}}{r} + \frac{A_{g1}}{r^2}\cos\theta + \frac{A_{g2}}{r^3}P_2(\cos\theta) + \frac{A_{g3}}{r^4}P_3(\cos\theta) \tag{34}$$

After fitting the Fluent data to this expression, Table 1 compares the coefficients determined against the analytical model.

Table 1. Analytical vs Numerical Coefficients

Coeff A_{gn}	Analytical Model $[Km^{(n+1)}]$	Ansys Fluent $[Km^{(n+1)}]$	Difference
A_{g0}	$2.886E-3$	$2.756E-3$	4.7 %
A_{g1}	$-3.742E-9$	$-3.712E-9$	0.8 %
A_{g2}	–	$5.123E-14$	NA
A_{g3}	–	$-1.477E-20$	NA

The differences between the numerical and analytical coefficients are under 5%. The larger error in A_{g0} is partially due to the finite dimension of the gas domain in the Fluent simulation (20 particle diameters), which doesn't accurately represent the boundary conditions at infinity.

The driving force of photophoresis is the thermal creep phenomenon, which is the only term in the velocity boundary condition at the particle surface when $Kn \longrightarrow 0$. As defined in Eq. (29), the thermal creep is proportional to the angular derivative of the gas temperature, $dT_g/d\theta$, at the particle surface. To further validate the model, this important derivative is also extracted from the Fluent solver and compared with the analytical derivative of Eq. (34) considering 1, 2 and 3 terms, as depicted in Fig. 2.

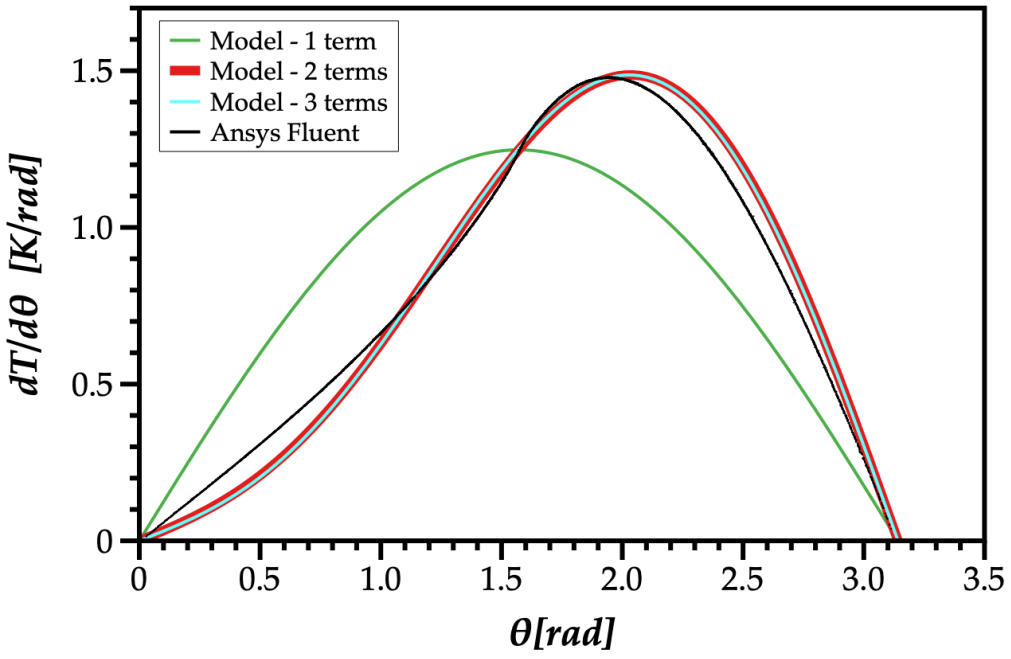

Figure 2. Evolution of temperature angular derivative with angle θ and comparison between a single term, two and three terms.

The figure shows that there is no need to calculate this derivative beyond the second term and that the numerical derivative is very similar to the analytical one. The small discrepancy might be due to numerical errors and finite boundary condition proximity in the numerical model.

3.2. Fluid flow part

The thermal creep boundary condition at the particle surface creates a velocity slip. The modeling of this condition in Ansys Fluent implied selecting the "no slip" boundary condition with a moving wall, where the velocity of the wall was defined using a custom expression for the thermal creep phenomenon. The derivative $dT_g/d\theta$ was extracted from the solver using the built-in gradient function. The results are presented in Table (2).

Table 2. Analytical vs. Numerical Photophoretic Force values

	Analytical Model	Ansys Fluent	Difference
$F_{ph}\ [pN]$	25.11	25.44	1.3 %

To further prove that the terms of degree higher than one do not contribute to the photophoretic force, the boundary condition expression was modified afterward, using the analytical derivative and removing the second and third terms. The photophoretic force value did not change significantly. We also tried only including the second and third-degree terms in the boundary conditions and magnified their magnitude. In that case, the produced force was negligible. Therefore, the model only requires A_{g0} and A_{g1}. The following section details the MATLAB algorithm developed to implement the model.

4. Model results and discussion

Most of the model expressions are straightforward to compute, with the exception of the A_{g0}, $F1$, and $F2$ integrals. Due to the lack of an analytical solution for $F1$ and $F2$, we followed a numerical approach (trapezoidal rule) for all the integrals. The heat source function q_g was computed in a point grid inside the coated domain using Lorenz-Mie theory (Bohren & Huffman, 2008). Ladutenko et al. (2017) and Peña & Pal (2009) developed the multilayer algorithm implemented. The validation of the algorithm included reproducing the results in Fig.4 of Kaiser & Schweiger (1993), noting that one should swap the refractive indexes of the core and shell according to Suzuki & Lee (2013) (probably a typo). The integrals were also calculated using a grid with half the resolution to check for convergence.

The slip-flow correction coefficients used in the calculations were chosen based on typical values (Malai et al., 2012; Chang & Keh, 2012) for complete accommodation and are presented in Table 3:

Table 3. Slip-flow coefficients used

Coefficient	Value	Coefficient	Value	Coefficient	Value	Coefficient	Value
K_{TS}	1.152	K_t	2.179	K_m	1.131	K_h	1

The model will be applied to a practical example of a copper-coated glass bubble. The outer radius of the glass shell will be constant at $R_2 = 5\ \mu m$. The particle is subjected to a beam with an

irradiance of $I_0 = 1.41\ MW/m^2$ and wavelength $\lambda = 520\ nm$. The complex refractive index for the glass is $N_2 = 1.5$ and $N_3 = 0.995 + 2.61i$ for copper.

The thermal conductivity of the hollow core, glass shell, and copper coating were assumed to be $k_1 = 0.0242\ W \cdot m^{-1}K^{-1}, k_2 = 1.05\ W \cdot m^{-1}K^{-1}$ and $k_3 = 398\ W \cdot m^{-1}K^{-1}$, respectively. The surrounding air is at atmospheric pressure and undisturbed flow temperature of $T_\infty = 300K$. The thermal conductivity, dynamic viscosity, and density of the air were evaluated at T_∞.

Fig. 3 plots the photophoretic force evolution as a function of the copper coating thickness for multiple glass shell thicknesses (keeping in mind that the outer shell radius R_2 is constant).

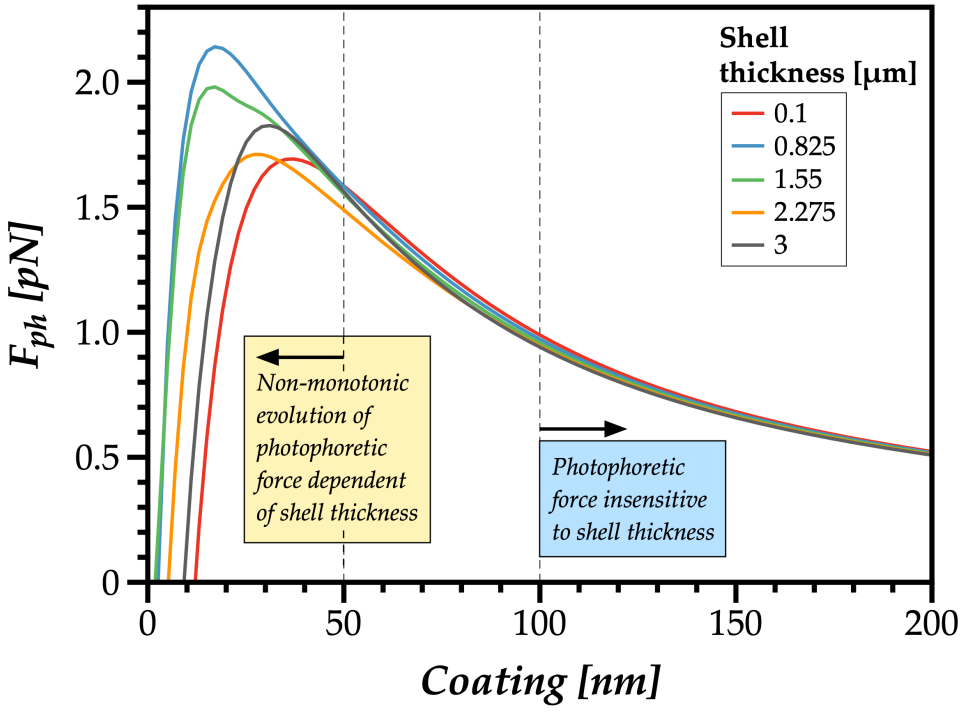

Figure 3. Photophoretic force vs. coating thickness for several shell thicknesses.

Before analyzing the results, it is important to remember that the fundamental driving mechanism of photophoresis is a thermal gradient in the surface of the particle. That gradient increases with the asymmetry of the heat generation and decreases with the thermal conductivity of the particle.

Fig. 3 shows that for a constant shell thickness, the photophoretic force increases rapidly with the coating thickness, reaching a maximum. This initial force increase is due to the increase in radiation absorption at the back of the particle (negative z, see Fig. 1) caused by the "growth" of the absorbing coat. At this point, this higher heat generation asymmetry is more substantial than increasing the thermal conductivity due to the metal coating.

However, as the coating thickens, the radiation absorbed plateaus and the high thermal conductivity of the copper begins to dominate the process, reducing the thermal gradient and, consequently, the photophoretic force.

The plots in Fig. 3 also show that, for copper coatings above $100\ nm$, the photophoretic force is

insensitive to the shell thickness. This insensitivity is expected considering the copper coating dominates both optical and thermal phenomena: thick copper coatings attenuate all the radiation before it reaches the shell (so the shell ceases to influence the electromagnetic fields), and the metal coating also conducts most of the heat through the particle.

Another important behavior to report is the non-monotonic evolution of the photophoretic force when the coating thickness is constant, which is more pronounced for thinner coatings ($< 50\ nm$). This effect may be due to the complex interaction between the multilayered particle and the electromagnetic field, which results in complicated dependencies. That complexity may also be responsible for the different curve shapes.

Table 4 shows how the photophoretic force maximum changes with the shell thickness. As expected, the values of the maximum value of F_{ph} and the corresponding coating thickness do not seem correlated with the shell thickness. In practice, applying a coating with such a precise thickness might not be achievable with current coating technologies. If one is unable to control the thickness of the deposited coating precisely, the results from Fig. (3) reveal that it is better to deposit in excess because the photophoretic force decreases at a lower rate after the maximum.

Table 4. Photophoretic force maxima

Shell thickness [μm]	$F_{ph,max}[pN]$	@coatingthickness [nm]
0.1	1.693	37.18
0.825	2.142	17.08
1.55	1.981	17.08
2.275	1.711	27.13
3	1.827	31.15

5. Conclusions

This work presents the development of a photophoresis model for a three-layered microsphere in the slip-flow regime, where the Navier-Stokes equations are applicable with corrected boundary conditions to account for temperature and velocity field discontinuities. The model expressions are mostly straightforward to compute, except for the terms involving integrals for which there is no analytical solution. Therefore, we used a numerical approach to overcome this challenge. The heat source function q_g computation used Lorenz-Mie theory and was validated using the coherence of the results with those obtained by numerical modeling.

The photophoretic model applied to a copper-coated glass bubble with an outer shell radius of $5\ \mu m$, considered the equivalent to a uniform laser beam with an irradiance of $1.41\ MW/m^2$ and a wavelength of $520\ nm$. The analysis of the photophoretic force as a function of the copper coating thickness considered different glass shell thicknesses. Results indicate that thicker coatings in the nanometric scale enhance the photophoretic force up to a maximum before decreasing due to the dominance of the high thermal conductivity of copper. For coatings above $100\ nm$, the pho-

tophoretic force becomes insensitive to shell thickness, highlighting the dominance of the copper coating in both optical and thermal phenomena.

The study also reveals a non-monotonic evolution of the photophoretic force with coating thickness, attributed to the complex interaction between the multilayered particle and the electromagnetic field. The findings suggest that considering the manufacturing precision of current coating technologies, in practice, it is better to deposit an excess coating to achieve higher photophoretic forces. The model and its insights provide a valuable theoretical and computable framework for optimizing the design of microparticles for photophoretic applications.

Ongoing work includes further validation of this model by comparing it against a more general numerical model (for Continuum and Slip-flow, $0 \leq Kn \leq 0.1$) and laboratory experiments. Also, to facilitate the application of this model, future work includes finding analytical solutions for the F1 and F2 integrals using Lorenz-Mie Theory.

Acknowledgements

The authors would like to acknowledge the *Fundação para a Ciência e Tecnologia* (FCT) for partially financing the research through projects UIPD/50022/2020 (DOI: 10.54499/UIDP/50022/2020) and UIDB/50022/2020 (DOI: 10.54499/UIDB/50022/2020). D. Pereira would like to acknowledge FCT and *Fundo Social Europeu* for the studentship 2022.12713.BD.

A. Relations for the scales in the boundary coefficients A_{g0} and A_{g1}

$$G1 = (k_1(2k_3(-R_1^3 + R_2^3) + k_2(2R_1^3 + R_2^3)) - 2k_2(1 + Kn_hK_t)(k_2(R_1^3 - R_2^3) - k_3(R_1^3 + 2R_2^3))) \tag{35}$$

$$G2 = (-k_1(k_3(R_1^3 - R_2^3) + k_2(2R_1^3 + R_2^3)) + k_2(1 + Kn_iK_t)(2k_2(R_1^3 - R_2^3) + k_3(R_1^3 + 2R_2^3))) \tag{36}$$

$$D1 = k_2(2R_1^3 + R_2^3)(2k_g(-R_2^3 + R_3^3) + k_3(1 + 2KnK_t)(2R_2^3 + R_3^3)) \tag{37}$$

$$D2 = 2k_3(R_1^3 - R_2^3)(k_3(1 + 2KnK_t)(R_2^3 - R_3^3) - k_g(R_2^3 + 2R_3^3)) \tag{38}$$

$$D3 = k_2(R_1^3 - R_2^3)(2k_g(-R_2^3 + R_3^3) + k_3(1 + 2KnK_t)(2R_2^3 + R_3^3)) \tag{39}$$

$$D4 = k_3(R_1^3 + 2R_2^3)(k_3(1 + 2KnK_t)(R_2^3 - R_3^3) - k_g(R_2^3 + 2R_3^3)) \tag{40}$$

References

Bera, S. K., Kumar, A., Sil, S., Saha, T. K., Saha, T., & Banerjee, A. (2016). Simultaneous measurement of mass and rotation of trapped absorbing particles in air. *Optics letters*, *41*(18), 4356–4359.

Bohren, C. F., & Huffman, D. R. (2008). *Absorption and scattering of light by small particles*. John Wiley & Sons.

Brock, J. R. (1962). On the theory of thermal forces acting on aerosol particles. *Journal of Colloid Science*, *17*(8), 768–780.

Chang, Y. C., & Keh, H. J. (2012). Effects of thermal stress slip on thermophoresis and photophoresis. *Journal of Aerosol Science*, *50*, 1–10.

Eckerskorn, N., Bowman, R., Kirian, R. A., Awel, S., Wiedorn, M., Küpper, J., ... Rode, A. V. (2015). Optically induced forces imposed in an optical funnel on a stream of particles in air or vacuum. *Physical Review Applied*, *4*(6), 064001.

Kaiser, T., & Schweiger, G. (1993). Stable algorithm for the computation of mie coefficients for scattered and transmitted fields of a coated sphere. *Computers in Physics*, *7*(6), 682–686.

Ladutenko, K., Pal, U., Rivera, A., & Peña-Rodríguez, O. (2017). Mie calculation of electromagnetic near-field for a multilayered sphere. *Computer Physics Communications*, *214*, 225–230.

Lizana, A., Zhang, H., Turpin, A., Van Eeckhout, A., Torres-Ruiz, F. A., Vargas, A., ... Campos, J. (2018). Generation of reconfigurable optical traps for microparticles spatial manipulation through dynamic split lens inspired light structures. *Scientific Reports*, *8*(1), 11263.

Loesche, C., & Husmann, T. (2016). Photophoresis on particles hotter/colder than the ambient gas for the entire range of pressures. *Journal of Aerosol Science*, *102*, 55–71.

Mackowski, D. (1989). Photophoresis of aerosol particles in the free molecular and slip-flow regimes. *International Journal of Heat and Mass Transfer*, *32*(5), 843–854.

Malai, N., Limanskaya, A., Shchukin, E., & Stukalov, A. (2012). Photophoresis of heated moderately large spherical aerosol particles. *Atmospheric and Oceanic Optics*, *25*(5), 355–363.

Peña, O., & Pal, U. (2009). Scattering of electromagnetic radiation by a multilayered sphere. *Computer Physics Communications*, *180*(11), 2348–2354.

Pereira, D., & Panão, M. (2022). Photophoresis of spherical particles in slip-flow regime. *Physics of Fluids*, *34*(10), 103307.

Rogers, W., Laney, J., Peatross, J., & Smalley, D. (2019). Improving photophoretic trap volumetric displays. *Applied optics*, *58*(34), G363–G369.

Shvedov, V. G., Desyatnikov, A. S., Rode, A. V., Krolikowski, W., & Kivshar, Y. S. (2009). Optical guiding of absorbing nanoclusters in air. *Optics Express*, *17*(7), 5743–5757.

Smalley, D., Nygaard, E., Squire, K., Van Wagoner, J., Rasmussen, J., Gneiting, S., ... others (2018). A photophoretic-trap volumetric display. *Nature*, *553*(7689), 486–490.

Suzuki, H., & Lee, I.-Y. S. (2013). Mie scattering field inside and near a coated sphere: computation and biomedical applications. *Journal of Quantitative Spectroscopy and Radiative Transfer*, *126*, 56–60.

Yalamov, Y., & Khasanov, A. (1998). Photophoresis of coarse aerosol particles with nonuniform thermal conductivity. *Technical Physics*, *43*(4), 347-352. (cited By 7) doi: 10.1134/1.1258984